

Polariton Dynamics in Two-Dimensional Ruddlesden–Popper Perovskites Strongly Coupled with Plasmonic Lattices

Jeong-Eun Park, Rafael López-Arteaga, Alexander D. Sample, Charles R. Cherqui, Ioannis Spanopoulos, Jun Guan, Mercouri G. Kanatzidis, George C. Schatz, Emily A. Weiss, and Teri W. Odom*



Cite This: *ACS Nano* 2022, 16, 3917–3925



Read Online

ACCESS |



Metrics & More



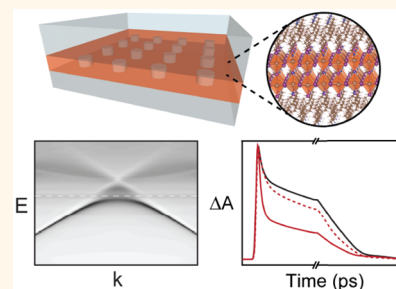
Article Recommendations



Supporting Information

ABSTRACT: Strong coupling between light and matter can produce hybrid eigenstates known as exciton–polaritons. Although polariton dynamics are important photophysical properties, the relaxation pathways of polaritons in different coupling regimes have seen limited attention. This paper reports the dynamics of hybridized states from 2D Ruddlesden–Popper perovskites coupled to plasmonic nanoparticle lattices. The open cavity architecture of Al lattices enables the coupling strength to be modulated by varying either the lead halide perovskite film thickness or the superstrate refractive index. Both experiments and finite-difference time-domain simulations of the optical dispersion diagrams showed avoided crossings that are a signature of strong coupling. Our analytical model also elucidated the correlation between the exciton/plasmon mixing ratio and polariton coupling strength. Using fs-transient absorption spectroscopy, we found that both the upper and lower polaritons have shorter lifetimes than the excitons and that polaritons can show faster excited-state dynamics when they have access to additional energy transfer channels.

KEYWORDS: strong coupling, polariton, plasmonic nanoparticle lattices, 2D perovskite, polariton dynamics



Exciton–polaritons, quasiparticles associated with the hybridization of excitons and photons, are driving advances in polariton chemistry, nonlinear physics, and quantum electrodynamics.^{1–5} Because light–matter mixing is possible with different time scales,⁶ understanding the effect of coupling on excited-state dynamics is important for applications of strongly coupled systems. When organic emitters such as J-aggregates with lifetimes on the ps/ns time scales hybridize with cavities such as gold gratings that show much faster decay rates (tens of fs), the coupled system usually supports polariton lifetimes that are faster than their uncoupled excitons.⁷ Upper polaritons tend to decay faster than lower polaritons because of faster thermal relaxation; the decay rates of lower polaritons, however, are more complicated and depend on the detailed energy states of the system.^{8,9} The presence of trapped states or phonon bottleneck effects can also limit excited-state decay channels and extend lifetimes of both upper and lower polaritons beyond those of the uncoupled exciton and cavity modes.^{10–13}

Recently, two-dimensional (2D) hybrid organic–inorganic perovskites have emerged as an attractive optoelectronic material for quantum information and communication studies.^{14,15} Their multiple quantum-well structures composed of inorganic slabs separated by organic cations support both strong quantum and dielectric confinement, resulting in large

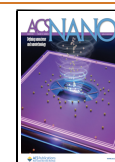
oscillator strengths and exciton binding energies ($E_b = 100–400$ meV).^{14,16,17} 2D lead halide perovskites with phenylethylamine ((PEA)₂PbX₄ where PEA \equiv C₆H₅C₂H₄NH₃⁺ and X = Br or I) strongly coupled with Fabry–Pérot (FP) cavities^{18–21} have shown polariton lasing²¹ at room temperature. Single-crystalline 2D perovskites without an external cavity but structured with flat surfaces that support optical modes can also exhibit strong polariton–polariton interactions.²² Despite the demonstration of polariton formation and their collective properties, the excitation dynamics of strongly coupled 2D perovskites are less known.

2D plasmonic nanoparticle (NP) lattices have an open cavity architecture that can mediate strong light–matter interactions.^{23–31} In a uniform refractive index environment, periodically arranged plasmonic NPs with an optimized photonic spacing exhibit surface lattice resonances (SLRs)^{32,33} with high quality factors Q (>400)³⁴ and relatively

Received: October 20, 2021

Accepted: February 18, 2022

Published: March 2, 2022



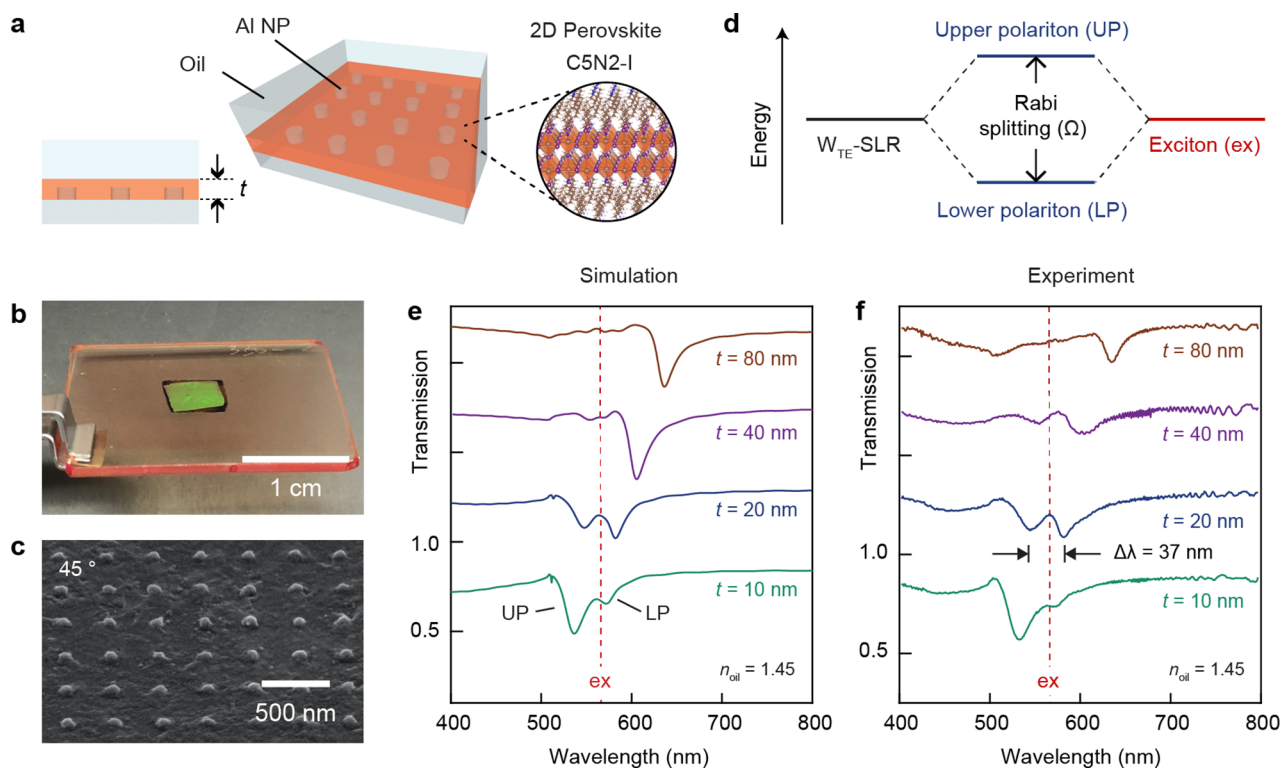


Figure 1. Structure and transmission spectra of C5N2-I film-coated Al NP lattices. (a) Scheme of C5N2-I film-coated Al NP lattices. (b) Photograph of Al NP lattices with a 20 nm thick C5N2-I film. (c) Scanning electron micrograph of 20 nm thick film-coated Al NP lattices at 45°. (d) Simplified energy diagram explaining hybridization of $W_{\text{TE-SLR}}$ and exciton modes, resulting in the formation of upper and lower polaritons separated by Rabi splitting. (e) Simulated transmission spectra of lattices with different perovskite film thicknesses. The refractive index of oil is 1.45. (f) Experimental transmission spectra under the same conditions as part e. All spectra in parts e and f are shown with the signal from not strongly coupled perovskites removed and are offset manually for better presentation. Dashed red lines depict the perovskite exciton mode.

long, few-ps lifetimes.^{35–37} When the superstrate/substrate index is highly mismatched such that waveguide conditions are met, NP lattices can support waveguide-coupled SLRs (W -SLRs); $W_{\text{TE-SLR}}$ and $W_{\text{TM-SLR}}$ result from coupling between SLRs and transverse electric (TE) and transverse magnetic (TM) waveguide modes, respectively.^{38,39} Since SLR properties can be tuned by lattice design and refractive index,^{40–44} NP lattices offer more opportunities than FP cavities for tailoring polariton properties, such as spatial coherence or group velocity.^{25,45,46} Moreover, since NP lattices show negligible absorption at most energies except at the SLR and localized plasmon wavelengths, they enable a wider range of wavelengths for ultrafast time-resolved studies compared to FP cavities having distributed Bragg reflectors.^{32,47}

Here, we report the dynamics of hybridized states from 2D Ruddlesden–Popper (RP) lead iodide perovskites strongly coupled to plasmonic Al NP lattices. The formation of exciton–polaritons was confirmed by Rabi splitting in the optical transmission spectra and anticrossing behavior in the dispersion diagrams. The coupling strength was first tuned by perovskite film thickness, with the experiment agreeing with finite-difference time-domain (FDTD) simulations. By changing the superstrate refractive index, we achieved more precise as well as reversible control over the degree of coupling, and the W -SLR/exciton mixing ratios of the polaritons were characterized by an analytical model. Finally, ultrafast transient absorption spectroscopy revealed that both upper and lower polaritons have faster excited-state dynamics compared to pristine excitons.

RESULTS AND DISCUSSION

Figure 1a depicts the scheme of our system composed of an Al NP lattice and a 2D perovskite, $(\text{PA})_2(\text{MA})\text{Pb}_2\text{I}_7$ ($\text{PA} = \text{CH}_3(\text{CH}_2)_4\text{NH}_3^+$, $\text{MA} = \text{CH}_3\text{NH}_3^+$). Since the number (n) of inorganic layers is 2, we denote the perovskite as C5N2-I by convention.⁴⁸ We fabricated square Al NP lattices with spacing $a_0 = 350$ nm, diameter $d = 70$ nm, and height $h = 60$ nm on fused silica using SANE and PEEL (Methods and Experimental Section).^{49–51} We selected Al because Al NP lattices can support SLRs that are higher-quality than those that Au or Ag NP lattices can support at wavelengths below 600 nm.⁵² At normal incidence ($\theta = 0^\circ$), bare Al NP lattices with an oil ($n_{\text{oil}} = 1.45$) superstrate index matched to the silica substrate supported a Γ -point SLR at 517 nm (Figure S1).

Perovskite precursor solutions in dimethylformamide spin-cast on the NP lattices formed C5N2-I thin films over cm^2 areas (Figure 1b). Scanning electron microscopy (Figure 1c) and atomic force microscopy (Figure S2) confirmed the conformal nature of the perovskite films. Increased concentrations of precursor solution (from 2.5% to 20%) resulted in film thicknesses (t) from ~ 10 to ~ 80 nm (Figure S3); X-ray powder diffraction patterns matched calculated C5N2-I, with thicker films having higher crystallinity (Figure S4). The transmission spectra of C5N2-I perovskite films on silica substrates showed a strong excitonic resonance at 568 nm from the $n = 2$ inorganic layers and a weak resonance at 610 nm from a small fraction of $n = 3$ layers (Figure S5).⁴⁸

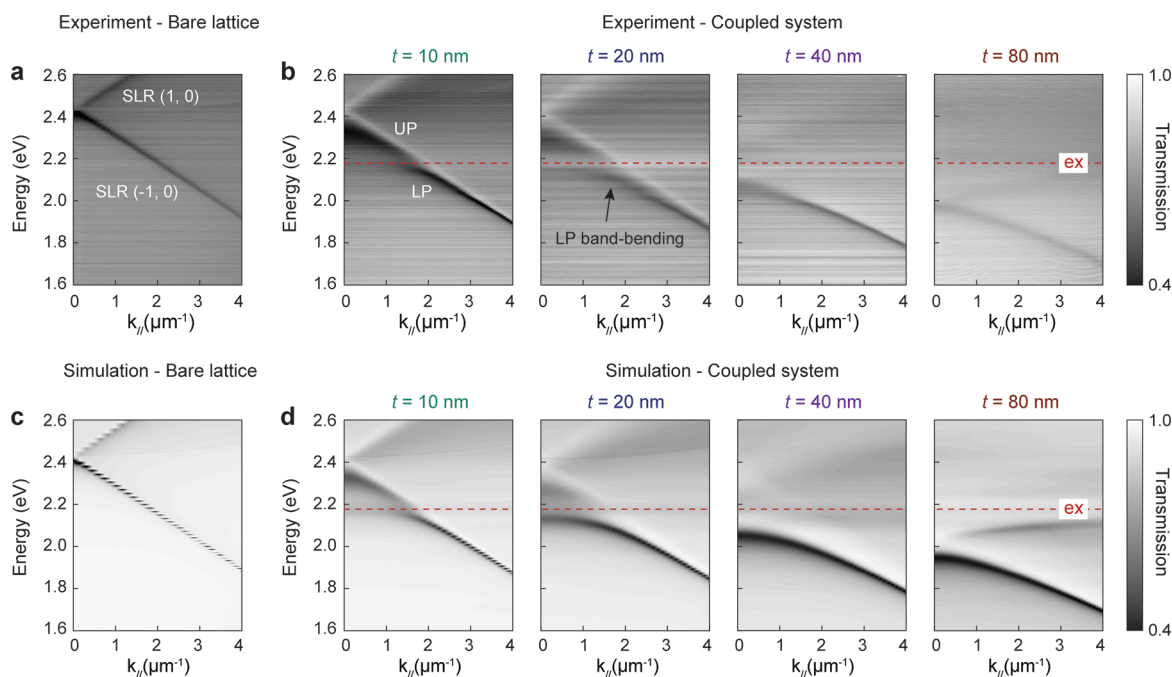


Figure 2. Optical band structures in $W_{\text{TE}}\text{-SLR}$ –exciton hybrid systems. Experimental angle-resolved transmission of (a) bare Al NP lattices with spacing $a_0 = 350$ nm, diameter $d = 70$ nm, and height $h = 60$ nm and (b) lattices with different film thicknesses under s-polarized light ($n_{\text{oil}} = 1.45$). Simulated spectra of (c) bare Al NP lattices and (d) lattices under the same environment as in part b. Dashed red lines in parts b and d depict the perovskite exciton mode. It should be noted that the signal from unhybridized perovskites was removed in parts b and d.

FDTD simulations with a Lorentz model allow for selective manipulation of excitonic materials via the oscillator strength S that quantifies the probability of excitonic absorption (see the [Methods](#) section in the Supporting Information). When perovskite films with $S = 0$ are added on top of the plasmonic NP lattices, uncoupled W-SLRs are formed due to the relatively high refractive index of the perovskite film ($n_{\text{film}} \sim 2.26$ @ 568 nm) (Figure S6). As t is increased, the effective refractive index of the waveguide mode increases, and the W-SLRs shift to longer wavelengths (Figure S7a). From the calculated near-field distributions, we confirmed that $W_{\text{TE}}\text{-SLRs}$ resemble pure SLRs while $W_{\text{TM}}\text{-SLRs}$ have stronger waveguide effects (Figure S7b). In this study, the $W_{\text{TE}}\text{-SLRs}$ hybridize with exciton modes to form upper polariton (UP) and lower polariton (LP) states with an energy separation known as the Rabi splitting (Ω) (Figure 1d).

FDTD simulations using empirically determined optical constants show transmission spectra with peak splitting at $t = 10, 20,$ and 40 nm (Figure 1e; the dashed red line at 568 nm is the exciton wavelength). It should be noted that we removed the signal from perovskites not hybridized with the NP lattice by subtraction (see the [Methods](#) section in the Supporting Information). Experimental results agreed with simulations; in the $t = 20$ nm film, where W-SLR–exciton detuning is the smallest among four thicknesses, the coupling is expected to be the strongest, with the measured wavelength difference $\Delta\lambda = 37$ nm corresponding to $\Delta E = 143$ meV (Figure 1f). Since our perovskite films can be readily removed from the NP lattices by dissolution in hexane, we used the same NP lattice to compare thickness effects of the perovskite films. The relative intensities of the UP and LP features can be changed by small differences in film thickness (18–22 nm) (Figure S8).

Angle-resolved transmission measurements revealed how the optical band structure of the NP lattices changed after coupling to the perovskite films. Under s-polarization, bare Al NP

lattices support two dispersive SLR bands⁵³ (Figure 2a). Figure 2b depicts that an Al NP lattice coupled to a $t = 10$ nm perovskite film showed two polariton bands with an avoided crossing, where the LP bends ca. $k_{\parallel} \sim 2 \mu\text{m}^{-1}$. Bending was more pronounced for $t = 20$ nm films at ca. $k_{\parallel} \sim 1.5 \mu\text{m}^{-1}$ when the LP approached the exciton energy. As t increased more, the higher effective refractive index of the perovskites continuously moved the $W_{\text{TE}}\text{-SLR}(-1, 0)$ to lower energies. For $t = 80$ nm films, the $W_{\text{TE}}\text{-SLR}$ shifted beyond the exciton energy, and strong coupling with the $(-1, 0)$ mode was no longer possible. The UP band for $t = 40$ and 80 nm films could not be resolved because of the strong perovskite absorption at higher energies.

FDTD-simulated dispersion diagrams showed hybridization between the plasmon mode and the exciton more clearly than the experiment. As expected, bare Al NP lattices support two linear dispersive bands (Figure 2c). The coupled systems with empirically determined perovskite optical constants showed clear LP band-bending approaching the exciton resonance (Figure 2d). The $t = 40$ nm case also showed some but less distinct bending near $k_{\parallel} = 0 \mu\text{m}^{-1}$. For the $t = 80$ nm film, the exciton mode could couple to the $W_{\text{TE}}\text{-SLR}(1, 0)$ mode at large k_{\parallel} . The quality factor Q of the polariton branches decreases as t increases since Q depends on the coupling between their parent modes, and the Q of uncoupled $W_{\text{TE}}\text{-SLRs}$ decreases at larger t . Simulated dispersions of Al NP lattices with a dielectric slab of the same index as the perovskite film only showed W-SLR bands (Figure S9), which confirms that the band-bending in Figure 2b,d originates from strong coupling between $W_{\text{TE}}\text{-SLR}$ and exciton modes.

The open geometry of plasmonic NP lattices offers a simple approach to tailor the coupling strength. Since the $W_{\text{TE}}\text{-SLR}$ wavelength depends on the surrounding index, detuning can be precisely and reversibly controlled by changing the superstrate refractive index n_{oil} at a given perovskite film thickness. Using

the same $t = 20$ nm film as in Figure 1f, we increased n_{oil} from 1.29 to 1.70 (Figure 3a). We observed a gradual shift of both

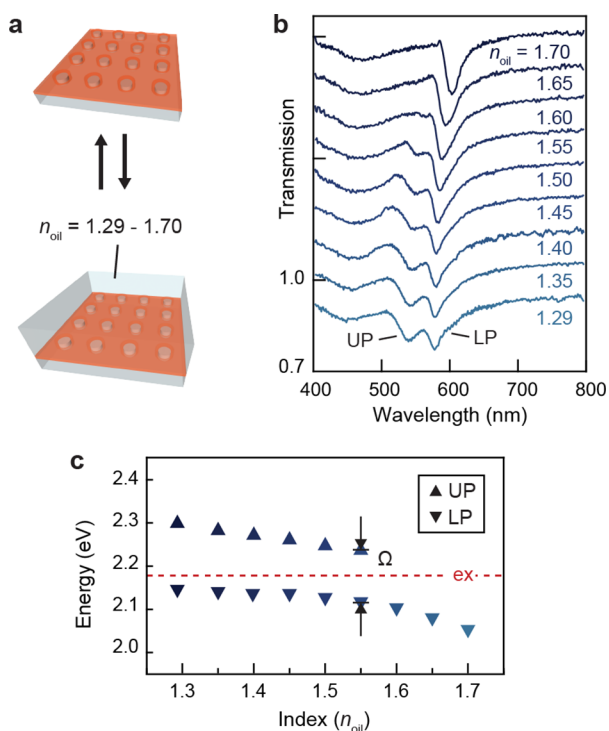


Figure 3. Precise control over the coupling strength and Rabi splitting. (a) Schematic illustration of repeated addition and removal of oil on top of the perovskite film. (b) Experimental transmission spectra of lattices with a 20 nm film at varied oil index values. (c) Energy of UP and LP extracted from part b.

the UP and LP to lower energies until the UP eventually disappeared at higher indices (Figure 3b). Anticrossing behavior between the UPs and LPs as a function of refractive index revealed $\Omega \sim 121$ meV at $n_{\text{oil}} = 1.55$ (Figure 3c). Simulated optical dispersion diagrams confirmed that the $W_{\text{TE-SLR}}$ at $k_{\parallel} = 0$ shifted to energies lower than the exciton at $n_{\text{oil}} = 1.70$ (Figure S10); hence, increasing n_{oil} from 1.55 to 1.70 tuned the coupling from stronger to weaker.

To analyze the coupling quantitatively and determine the relative contributions of the exciton and $W_{\text{TE-SLR}}$ in the polaritons as a function of refractive index, we first calculated the lattice–perovskite system without coupling (see the Methods section in the SI). With $S = 0$, only uncoupled $W_{\text{TE-SLR}}$ [$E_{\text{W-SLR}}(n_{\text{oil}})$] modes formed (Figure 4a). Using $S = 0.0725$, which yields the same splitting as in experiments ($\Omega \sim 121$ meV at $n_{\text{oil}} = 1.55$), we calculated the energies of the UP (E_{UP}) and LP (E_{LP}) at different indices (Figure 4b and Figure S11). As n_{oil} increased from 1.29 to 1.70, $E_{\text{W-SLR}}(n_{\text{oil}})$ (Figure 4c, dashed black line) shifted from 2.34 to 2.05 eV and crossed the exciton resonance at $n_{\text{oil}} = 1.55$. The E_{UP} and E_{LP} (\blacktriangle and \blacktriangledown in Figure 4c) agreed with the experiment (Figure 3c) and validated the Lorentz model for describing the excitonic character of our perovskite film.

Using an analytical two-state model (see the Methods section in the SI), we then built a linear response model from uncoupled modes to calculate the energies of the UP and LP branches (Figure 4c, solid lines):

$$E_{\text{UP,LP-branch}} = \frac{1}{2} \left[E_{\text{W-SLR}}(n_{\text{oil}}) + E_{\text{ex}} \pm \sqrt{4g^2 + \Delta(n_{\text{oil}})^2} \right]$$

where the detuning parameter $\Delta(n_{\text{oil}}) = E_{\text{W-SLR}}(n_{\text{oil}}) - E_{\text{ex}}$ and g is the coupling strength. The $g = 65$ meV value produced the best fit of the polariton branches with the FDTD-calculated $E_{\text{UP,LP}}$ and Rabi splitting ($\Omega \sim 2g$)⁵⁴ of ~ 131 meV at $n_{\text{oil}} = 1.55$. Adding losses to the model did not affect the energy eigenvalues because both the exciton and the W-SLR modes have relatively low losses, and damping is negligible in the overall energy of the system. From this model, we also determined the quantitative $W_{\text{TE-SLR}}$ and exciton mixing ratios of the polariton branches. At $n_{\text{oil}} = 1.55$, both UP and LP in the $t = 20$ nm film have equal contributions of $W_{\text{TE-SLR}}$ and the exciton. As n_{oil} increased from 1.29 to 1.70, the UP became mostly excitonic, and the $W_{\text{TE-SLR}}$ character decreased from $\sim 88\%$ to $\sim 15\%$ (Figure 4d, top); in contrast, the LP became mostly photonic, and the $W_{\text{TE-SLR}}$ character increased from $\sim 12\%$ to $\sim 85\%$ (Figure 4d, bottom).

Finally, using ultrafast transient absorption (TA) spectroscopy, we compared how tuning of the coupling strength by either perovskite film thickness or superstrate index affected energy relaxation of the polaritons. Figure 5a shows the TA spectra of pristine perovskite films of different thicknesses pumped with a 410 nm fs laser and probed between 390 and 700 nm. The most prominent features are ground state bleaching (GSB) at 570 nm (from $n = 2$ perovskites) and 610 nm (from $n = 3$ perovskites), which is consistent with the excitonic features in the steady-state transmission spectra (Figure S5). Although the exciton bleach for the $n = 2$ perovskite reached a maximum amplitude at 0.5 ps, the signal from the $n = 3$ was strongest at 1 ps. This slower rise of the bleach for $n = 3$ (Figure S12) is likely from an energy cascade in 2D perovskite films that funnels the photoexcitation from higher-energy states ($n = 2$) to lower-energy states ($n = 3$).^{55,56} The bleaches overlaid a broad excited state absorption (ESA) that spans much of the visible spectrum (<560 , ~ 580 nm, and >620 nm).

In the lattice–perovskite systems (Figure 5b), we observed new GSB signals with the same energy as the polaritonic features in the steady-state measurement (Figure 1f). In the TA spectra of the $t = 10$, 40, and 80 nm films, we only resolved a new GSB from UP for $t = 10$ nm and LP for $t = 40$ and 80 nm, but not both because of the overwhelming GSB signal from nonhybridized perovskites. The $t = 20$ nm film shows the most distinct change; the intensity of the excitonic GSB at 568 nm decreased considerably, and two polaritonic GSBs at 550 nm (UP) and 584 nm (LP) clearly appeared, even with overlapped features from the uncoupled excitons. We also acquired TA spectra for $t = 20$ nm films at $n_{\text{oil}} = 1.29$ and 1.70, and both cases also showed either UP or LP features, but not both (Figure S13).

After scaling the kinetic profiles for comparison, we found that the dynamics of the UP, LP, and exciton show distinct differences in the first 10 ps and are indistinguishable after ~ 200 ps (Figure 6a, Figure S14). Although strongly coupled organic molecules and organometal halide perovskites used bi- and triexponential terms,^{57,58} we used tetra-exponential decays to best fit each kinetic trace (Table S1). Based on carrier dynamics of perovskite nanocrystals, 2D halide perovskite nanoplatelets, and 2D RP perovskites,^{48,59,60} each decay component can be assigned to exciton–exciton/polariton–polariton scattering, exciton–phonon/polariton–phonon scat-

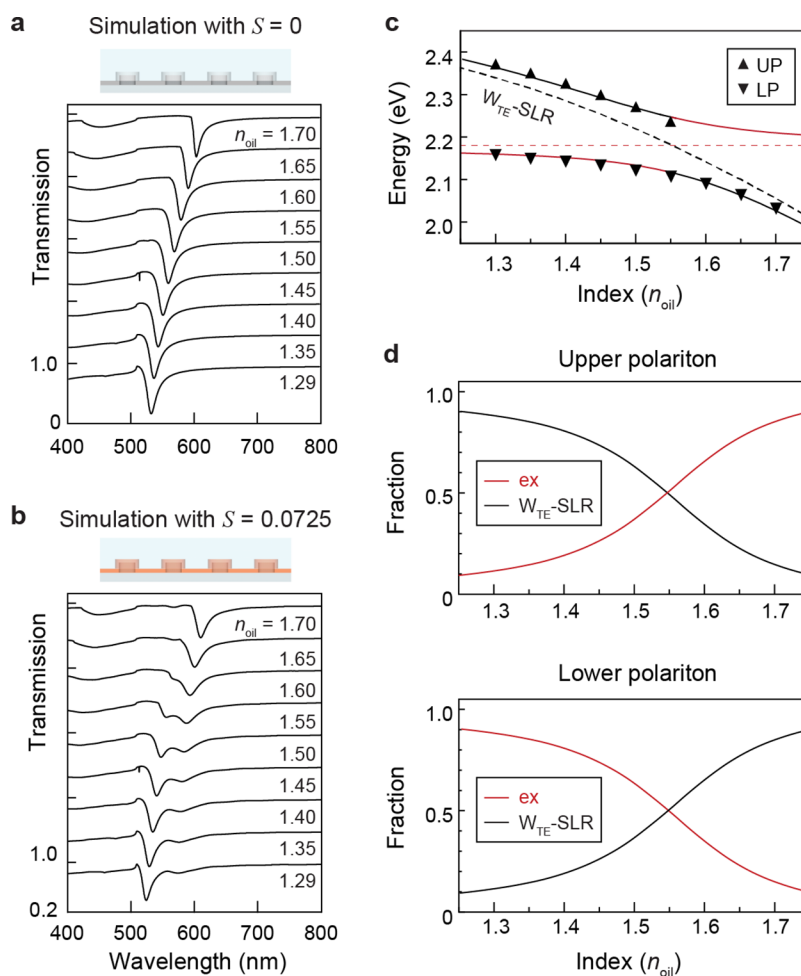


Figure 4. Interpretation of index-dependent coupling using FDTD simulation and a two-state model. Schematic illustrations and simulated transmission spectra of lattices with $t = 20$ nm for FDTD simulations when the oscillator strength is (a) $S = 0$ and (b) $S = 0.0725$ in the Lorentz model. (c) Index-dependent uncoupled $W_{\text{TE-SLR}}$ energies ($E_{W\text{-SLR}}$, dashed black line) and UP/LP energies (E_{UP} , E_{LP} , \blacktriangle and \blacktriangledown) obtained from FDTD simulations and UP/LP branches (solid lines) from a two-state model. (d) Relative mixing fraction of the exciton and $W_{\text{TE-SLR}}$ of the UP and LP branch as a function of index.

tering, Auger recombination, and radiative recombination from the fastest to slowest decay components ($\tau_1 - \tau_4$). Since these excitonic materials are similar to 2D RP perovskites, and polariton formation does not change available decay pathways for excited states, these assignments are consistent. We did not observe Rabi oscillations in the kinetic profiles due to the relatively long instrument response function (IRF) in our TA experiments (250 fs). The amplitude-averaged lifetimes of excitons increased as t increased from 10 to 80 nm (44 ± 3 to 125 ± 7 ps) (Figure 6b); this increase may be attributed to thinner films having lower crystallinity and a higher density of grain boundary defects that induce fast nonradiative decay.^{61,62} When excitons hybridize with $W_{\text{TE-SLR}}$ s, the polaritons have shorter lifetimes than their corresponding excitons, and experimentally, we only measured the lifetime of pure SLRs ($\sim 8.1 \pm 0.4$ ps) (Table S2). The reduction of lifetime was most significant in the $t = 20$ nm film, with the LP having a lifetime of 24 ± 2 ps and the exciton 52 ± 3 ps. This result is unexpected because the LP at $t = 20$ nm has a smaller contribution from the $W_{\text{TE-SLR}}$ than other UPs and LPs observed in TA spectra (Figure S15 and Table S3). This faster relaxation suggests additional relaxation pathways, such as energy transfer from the LP to the $n = 3$ exciton mode since their energy difference is small. This observation is consistent

with previous work,⁶³ where a smaller energy gap between polaritonic and nonpolaritonic states enabled faster decay of LPs through ultrafast internal conversion in molecules. For perovskite films surrounded by different indices, the UP of $t = 20$ nm films at $n_{\text{oil}} = 1.29$ and the LP at $n_{\text{oil}} = 1.70$ both have over 80% $W_{\text{TE-SLR}}$ (Figure 4d). However, while the UP at $n_{\text{oil}} = 1.29$ decayed faster compared to the exciton (from 64 ± 6 to 26 ± 1 ps), the LP at $n_{\text{oil}} = 1.70$ exhibited a longer lifetime (from 65 ± 6 to 91 ± 1 ps) (Figure S16). The extended lifetime may be attributed to a phonon bottleneck,⁸ but further work is required to explain why the effect is observed only for the LP at $n_{\text{oil}} = 1.70$.

CONCLUSIONS

In summary, we investigated strong coupling between 2D hybrid perovskites and plasmonic NP lattices and their polariton dynamics. Tailoring the coupling strength controlled the energy difference between the LPs and excitons, which resulted in polariton lifetimes as fast as half that of pristine excitons because of additional ultrafast energy transfer pathways. The observed polariton dynamics enables the design of hybrid-emitter systems that exhibit desirable photophysics properties for diverse applications, including solar cells, where

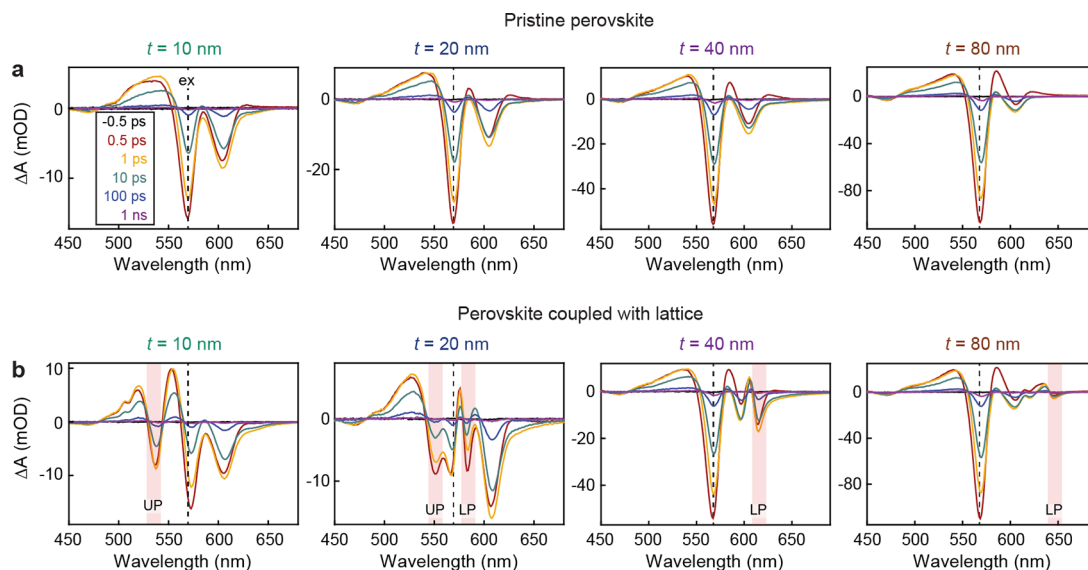


Figure 5. Transient absorption spectra of perovskites with and without coupling to lattices. Spectra of (a) pristine perovskites and (b) perovskites coupled with Al NP lattices at $n_{\text{oil}} = 1.45$ as a function of pump–probe delay time up to 3 ns. Polariton dips are marked as shaded areas. The pump excitation beam was tuned to 410 nm with 30 nJ per pulse. The pump–probe delay times in panel a apply to all panels. The signal from uncoupled excitons was not removed to avoid extraneous GSBs that may be introduced after subtraction due to the high sensitivity of TA spectra.

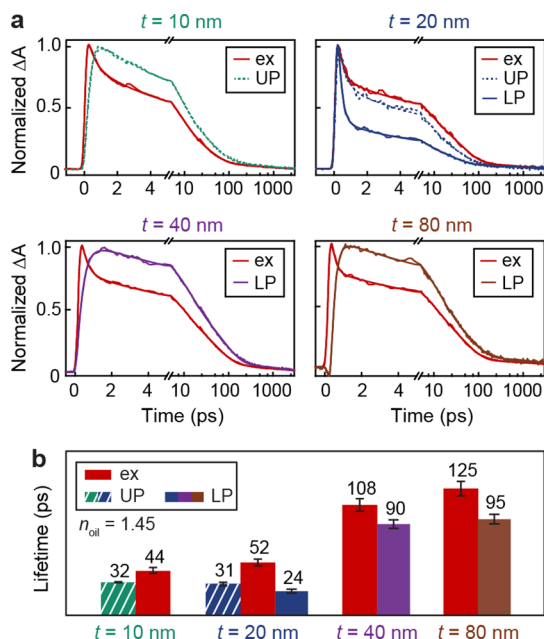


Figure 6. Polariton dynamics analysis. (a) Normalized kinetic profiles of excitons and polaritons for each film thickness at $n_{\text{oil}} = 1.45$. (b) Comparison of the amplitude-averaged lifetimes for UPs and LPs with those of their excitons.

longer excited-state lifetimes and diffusion are advantageous, and lasers, where faster radiative decay is beneficial. We believe that the open cavity architecture of 2D plasmonic NP lattices will facilitate the development of polariton devices with on-demand tunability.

METHODS/EXPERIMENTAL SECTION

Fabrication of Al NP Lattices. Al NP lattices were fabricated on fused silica by a soft nanofabrication process. We first make square-type periodic photoresist posts on Si wafers by solvent-assisted nanoscale embossing (SANE⁴⁹). Then, 8 nm thick Cr was deposited

by thermal evaporation, followed by the liftoff of photoresists and Si etching by reactive ion etching. Au deposition by thermal evaporator makes Au hole masks, and the Cr layer between the Si wafer and Au mask is removed by wet etching. We floated the Au hole masks on water and transferred them to a fused silica substrate. To fabricate Al NP lattices, we deposited 60 nm of Al through a Au hole mask, removed the Au hole mask with tape, and thermally annealed the sample⁶⁴ at 500 °C for 30 min.

C5N2-I Film Fabrication. Starting materials (single crystals of C5N2-I) were synthesized according to published procedures.⁴⁸ The crystals were filtered and dried under vacuum for 14 h. A suitable amount of dried crystals was dissolved in anhydrous dimethylformamide to create a final concentration of 2.5–20% (w/v). All substrates were pretreated for 10 min using the ultraviolet ozone (UVO) treatment method. Then, 40 μL of the precursor solution was spin-cast on the lattices at a speed of 3000 rpm for 1 min. The resulting films were then annealed at 100 °C on a hot plate for 30 s in air. Before transmission measurements, we added one drop of oil and covered it with thin microscope glass coverslips.

ASSOCIATED CONTENT

Supporting Information

The Supporting Information is available free of charge at <https://pubs.acs.org/doi/10.1021/acsnano.1c09296>.

Transmission spectra of bare Al nanoparticle lattices; atomic force micrographs of lattices without/with perovskite films; thickness of C5N2-I films; powder X-ray diffraction pattern of C5N2-I films; optical spectra of C5N2-I films; optical constants of C5N2-I films; simulation of waveguide-coupled SLRs; simulated transmission spectra with finely tuned thickness; simulated dispersion diagram of uncoupled W_{TE} -SLR bands; simulated dispersion diagram for $t = 20$ nm with two different index oils; optimization of S at $t = 20$ nm and $n_{\text{oil}} = 1.55$; kinetic profiles of exciton modes of $n = 2$ and $n = 3$ layers; TA spectra of pristine and coupled 20 nm films at $n_{\text{oil}} = 1.29$ and 1.70; kinetic profiles of 20 nm films at $n_{\text{oil}} = 1.29$ and 1.70; film-thickness-dependent splitting; lifetimes of 20 nm films at $n_{\text{oil}} = 1.29$ and 1.70;

fitting parameters for excitons and polaritons; fitting parameters for SLR; and film-thickness-dependent characteristics of polaritons ($n_{\text{oil}} = 1.45$) (PDF)

AUTHOR INFORMATION

Corresponding Author

Teri W. Odom – Department of Chemistry, Northwestern University, Evanston, Illinois 60208, United States; Department of Materials Science and Engineering, Northwestern University, Evanston, Illinois 60208, United States; orcid.org/0000-0002-8490-292X; Email: todom@northwestern.edu

Authors

Jeong-Eun Park – Department of Chemistry, Northwestern University, Evanston, Illinois 60208, United States; Present Address: Department of Chemistry, Gwangju Institute of Science and Technology (GIST), Gwangju 61005, Korea; orcid.org/0000-0002-6926-2696

Rafael López-Arteaga – Department of Chemistry, Northwestern University, Evanston, Illinois 60208, United States; orcid.org/0000-0001-8058-3469

Alexander D. Sample – Department of Chemistry, Northwestern University, Evanston, Illinois 60208, United States; orcid.org/0000-0002-4561-8619

Charles R. Cherqui – Department of Chemistry, Northwestern University, Evanston, Illinois 60208, United States; orcid.org/0000-0003-2818-7973

Ioannis Spanopoulos – Department of Chemistry, Northwestern University, Evanston, Illinois 60208, United States; Present Address: Department of Chemistry, University of South Florida, Tampa, Florida 33620, United States; orcid.org/0000-0003-0861-1407

Jun Guan – Department of Chemistry, Northwestern University, Evanston, Illinois 60208, United States; orcid.org/0000-0001-8667-1611

Mercouri G. Kanatzidis – Department of Chemistry, Northwestern University, Evanston, Illinois 60208, United States; orcid.org/0000-0003-2037-4168

George C. Schatz – Department of Chemistry, Northwestern University, Evanston, Illinois 60208, United States; orcid.org/0000-0001-5837-4740

Emily A. Weiss – Department of Chemistry, Northwestern University, Evanston, Illinois 60208, United States; Department of Materials Science and Engineering, Northwestern University, Evanston, Illinois 60208, United States; orcid.org/0000-0001-5834-463X

Complete contact information is available at: <https://pubs.acs.org/10.1021/acsnano.1c09296>

Author Contributions

J.-E.P. and T.W.O. conceived the idea of strong coupling of plasmonic nanoparticle lattices and 2D Ruddlesden–Popper perovskites. J.-E.P. prepared the plasmonic nanoparticle lattices and perovskite films, designed the investigation, and performed the steady-state characterizations. R.L.-A. performed the ultrafast transient absorption (TA) measurements, and J.-E.P. and R.L.-A. analyzed the TA data. A.D.S. participated in the steady-state characterization and TA data analysis. J.-E.P. performed the FDTD simulations with the help of C.R.C. who developed a two-state model. I.S. prepared the perovskite crystals and acquired powder X-ray diffraction patterns of

perovskite films. J.G. participated in the discussion. T.W.O., E.A.W., G.C.S., and M.K. guided the experimental and theoretical investigations. J.-E.P. and T.W.O. analyzed the data and wrote the manuscript. All authors commented on and revised the manuscript.

Notes

The authors declare no competing financial interest.

ACKNOWLEDGMENTS

This work was supported by the Vannevar Bush Faculty Fellowship from the US Department of Defense (DOD N00014-17-13023) and the Office of Naval Research (ONR N00014-21-1-2289). This work made use of the NUFAB facility and the EPIC facility of Northwestern University's NUANCE Center, which has received support from the SHyNE Resource (NSF ECCS-2025633), the IIN, and Northwestern's MRSEC program (NSF DMR-1720139). R.L.-A. and E.A.W. were supported by The Center for Molecular Quantum Transduction, an Energy Frontier Research Center funded by DOE, Office of Science, BES under Award DE-SC0021314. C.C. and G.C.S. were supported by the Department of Energy, Office of Basic Energy Science under grant DE-SC0004752. I.S. and M.G.K. were supported in part from the US Department of Energy, Office of Science Grant SC0012541.

REFERENCES

- (1) Ribeiro, R. F.; Martinez-Martinez, L. A.; Du, M.; Campos-Gonzalez-Angulo, J.; Yuen-Zhou, J. Polariton chemistry: controlling molecular dynamics with optical cavities. *Chemical Science* **2019**, *10* (46), 10822–10822.
- (2) Rivera, N.; Kaminer, I. Light-matter interactions with photonic quasiparticles. *Nature Reviews Physics* **2020**, *2* (10), 538–561.
- (3) Flick, J.; Rivera, N.; Narang, P. Strong light-matter coupling in quantum chemistry and quantum photonics. *Nanophotonics* **2018**, *7* (9), 1479–1501.
- (4) Su, R.; Diederichs, C.; Wang, J.; Liew, T. C. H.; Zhao, J. X.; Liu, S.; Xu, W. G.; Chen, Z. H.; Xiong, Q. H. Room-Temperature Polariton Lasing in All-Inorganic Perovskite Nanoplatelets. *Nano Lett.* **2017**, *17* (6), 3982–3988.
- (5) Su, R.; Fieramosca, A.; Zhang, Q.; Nguyen, H. S.; Deleporte, E.; Chen, Z. H.; Sanvitto, D.; Liew, T. C. H.; Xiong, Q. H. Perovskite semiconductors for room-temperature exciton-polaritons. *Nat. Mater.* **2021**, *20* (10), 1315–1324.
- (6) Wang, H.; Wang, H.-Y.; Sun, H.-B.; Cerea, A.; Toma, A.; De Angelis, F.; Jin, X.; Razzari, L.; Cojoc, D.; Catone, D.; Huang, F.; Proietti Zaccaria, R. Dynamics of Strongly Coupled Hybrid States by Transient Absorption Spectroscopy. *Adv. Funct. Mater.* **2018**, *28* (48), 1801761.
- (7) Vasa, P.; Pomraenke, R.; Cirmi, G.; De Re, E.; Wang, W.; Schwieger, S.; Leipold, D.; Runge, E.; Cerullo, G.; Lienau, C. Ultrafast Manipulation of Strong Coupling in Metal–Molecular Aggregate Hybrid Nanostructures. *ACS Nano* **2010**, *4* (12), 7559–7565.
- (8) Wang, H.; Wang, H. Y.; Sun, H. B.; Cerea, A.; Toma, A.; De Angelis, F.; Jin, X.; Razzari, L.; Cojoc, D.; Catone, D.; Huang, F. C.; Zaccaria, R. P. Dynamics of Strongly Coupled Hybrid States by Transient Absorption Spectroscopy. *Adv. Funct. Mater.* **2018**, *28* (48), 1870342.
- (9) Mrejen, M.; Yadgarov, L.; Levanon, A.; Suchowski, H. Transient exciton-polariton dynamics in WSe₂ by ultrafast near-field imaging. *Science Advances* **2019**, *5*, No. eaat9618.
- (10) Tassone, F.; Piermarocchi, C.; Savona, V.; Quattropani, A.; Schwendimann, P. Bottleneck effects in the relaxation and photoluminescence of microcavity polaritons. *Phys. Rev. B* **1997**, *56* (12), 7554–7563.

- (11) Tartakovskii, A. I.; Emam-Ismael, M.; Stevenson, R. M.; Skolnick, M. S.; Astratov, V. N.; Whittaker, D. M.; Baumberg, J. J.; Roberts, J. S. Relaxation bottleneck and its suppression in semiconductor microcavities. *Phys. Rev. B* **2000**, *62* (4), R2283–R2286.
- (12) Wang, H.; Wang, H. Y.; Bozzola, A.; Toma, A.; Panaro, S.; Raja, W.; Alabastri, A.; Wang, L.; Chen, Q. D.; Xu, H. L.; De Angelis, F.; Sun, H. B.; Zaccaria, R. P. Dynamics of Strong Coupling between J-Aggregates and Surface Plasmon Polaritons in Subwavelength Hole Arrays. *Adv. Funct. Mater.* **2016**, *26* (34), 6198–6205.
- (13) Wang, H.; Toma, A.; Wang, H. Y.; Bozzola, A.; Miele, E.; Haddadpour, A.; Veronis, G.; De Angelis, F.; Wang, L.; Chen, Q. D.; Xu, H. L.; Sun, H. B.; Zaccaria, R. P. The role of Rabi splitting tuning in the dynamics of strongly coupled J-aggregates and surface plasmon polaritons in nanohole arrays. *Nanoscale* **2016**, *8* (27), 13445–13453.
- (14) Zheng, K. B.; Pullerits, T. Two Dimensions Are Better for Perovskites. *J. Phys. Chem. Lett.* **2019**, *10* (19), 5881–5885.
- (15) Wang, H. Z.; Fang, C.; Luo, H. M.; Li, D. H. Recent progress of the optoelectronic properties of 2D Ruddlesden-Popper perovskites. *J. Semicond.* **2019**, *40* (4), 041901.
- (16) Blancon, J. C.; Stier, A. V.; Tsai, H.; Nie, W.; Stoumpos, C. C.; Traore, B.; Pedesseau, L.; Kepenekian, M.; Katsutani, F.; Noe, G. T.; Kono, J.; Tretiak, S.; Crooker, S. A.; Katan, C.; Kanatzidis, M. G.; Crochet, J. J.; Even, J.; Mohite, A. D. Scaling law for excitons in 2D perovskite quantum wells. *Nat. Commun.* **2018**, *9*, 2254.
- (17) Mao, L. L.; Stoumpos, C. C.; Kanatzidis, M. G. Two-Dimensional Hybrid Halide Perovskites: Principles and Promises. *J. Am. Chem. Soc.* **2019**, *141* (3), 1171–1190.
- (18) Lanty, G.; Brehier, A.; Parashkov, R.; Lauret, J. S.; Deleporte, E. Strong exciton-photon coupling at room temperature in microcavities containing two-dimensional layered perovskite compounds. *New J. Phys.* **2008**, *10*, 065007.
- (19) Fieramosca, A.; De Marco, L.; Passoni, M.; Polimeno, L.; Rizzo, A.; Rosa, B. L. T.; Cruciani, G.; Dominici, L.; De Giorgi, M.; Gigli, G.; Andreani, L. C.; Gerace, D.; Ballarini, D.; Sanvitto, D. Tunable Out-of-Plane Excitons in 2D Single-Crystal Perovskites. *ACS Photonics* **2018**, *5* (10), 4179–4185.
- (20) Wang, J.; Su, R.; Xing, J.; Bao, D.; Diederichs, C.; Liu, S.; Liew, T. C. H.; Chen, Z. H.; Xiong, Q. H. Room Temperature Coherently Coupled Exciton-Polaritons in Two-Dimensional-Organic Inorganic Perovskite. *ACS Nano* **2018**, *12* (8), 8382–8389.
- (21) Zhang, X. L.; Shi, H. F.; Dai, H. T.; Zhang, X. H.; Sun, X. W.; Zhang, Z. Y. Exciton-Polariton Properties in Planar Microcavity of Millimeter-Sized Two-Dimensional Perovskite Sheet. *ACS Appl. Mater. Interfaces* **2020**, *12* (4), 5081–5089.
- (22) Fieramosca, A.; Polimeno, L.; Ardizzone, V.; De Marco, L.; Pugliese, M.; Maiorano, V.; De Giorgi, M.; Dominici, L.; Gigli, G.; Gerace, D.; Ballarini, D.; Sanvitto, D. Two-dimensional hybrid perovskites sustaining strong polariton interactions at room temperature. *Science Advances* **2019**, *5* (5), 9967.
- (23) Rodriguez, S. R. K.; Rivas, J. G. Surface lattice resonances strongly coupled to Rhodamine 6G excitons: tuning the plasmon-exciton-polariton mass and composition. *Opt Express* **2013**, *21* (22), 27411–27421.
- (24) Vakevainen, A. I.; Moerland, R. J.; Rekola, H. T.; Eskelinen, A. P.; Martikainen, J. P.; Kim, D. H.; Torma, P. Plasmonic Surface Lattice Resonances at the Strong Coupling Regime. *Nano Lett.* **2014**, *14* (4), 1721–1727.
- (25) Ramezani, M.; Halpin, A.; Feist, J.; Van Hoof, N.; Fernandez-Dominguez, A. I.; Garcia-Vidal, F. J.; Rivas, J. G. Dispersion Anisotropy of Plasmon-Exciton-Polaritons in Lattices of Metallic Nanoparticles. *ACS Photonics* **2018**, *5* (1), 233–239.
- (26) Vakevainen, A. I.; Moilanen, A. J.; Necada, M.; Hakala, T. K.; Daskalakis, K. S.; Torma, P. Sub-picosecond thermalization dynamics in condensation of strongly coupled lattice plasmons. *Nat. Commun.* **2020**, *11* (1), 3139.
- (27) Yadav, R. K.; Otten, M.; Wang, W. J.; Cortes, C. L.; Gosztola, D. J.; Wiederrecht, G. P.; Gray, S. K.; Odom, T. W.; Basu, J. K. Strongly Coupled Exciton-Surface Lattice Resonances Engineer Long-Range Energy Propagation. *Nano Lett.* **2020**, *20* (7), 5043–5049.
- (28) Yadav, R. K.; Bourgeois, M. R.; Cherqui, C.; Juarez, X. G.; Wang, W. J.; Odom, T. W.; Schatz, G. C.; Basu, J. K. Room Temperature Weak-to-Strong Coupling and the Emergence of Collective Emission from Quantum Dots Coupled to Plasmonic Arrays. *ACS Nano* **2020**, *14* (6), 7347–7357.
- (29) Liu, W. J.; Lee, B.; Naylor, C. H.; Ee, H. S.; Park, J.; Johnson, A. T. C.; Agarwal, R. Strong Exciton-Plasmon Coupling in MoS₂ Coupled with Plasmonic Lattice. *Nano Lett.* **2016**, *16* (2), 1262–1269.
- (30) Lee, B.; Liu, W. J.; Naylor, C. H.; Park, J.; Malek, S. C.; Berger, J. S.; Johnson, A. T. C.; Agarwal, R. Electrical Tuning of Exciton-Plasmon Polariton Coupling in Monolayer MoS₂ Integrated with Plasmonic Nanoantenna Lattice. *Nano Lett.* **2017**, *17* (7), 4541–4547.
- (31) Wang, S. J.; Quynh, L. V.; Vaianella, F.; Maes, B.; Barker, S. E.; Godiksen, R. H.; Curto, A. G.; Rivas, J. G. Limits to Strong Coupling of Excitons in Multilayer WS₂ with Collective Plasmonic Resonances. *ACS Photonics* **2019**, *6* (2), 286–293.
- (32) Ramezani, M.; Berghuis, M.; Rivas, J. G. Strong light-matter coupling and exciton-polariton condensation in lattices of plasmonic nanoparticles [Invited]. *J. Opt. Soc. Am. B* **2019**, *36* (7), E88–E103.
- (33) Wang, W. J.; Ramezani, M.; Vakevainen, A. I.; Torma, P.; Rivas, J. G.; Odom, T. W. The rich photonic world of plasmonic nanoparticle arrays. *Mater. Today* **2018**, *21* (3), 303–314.
- (34) Deng, S.; Li, R.; Park, J.-E.; Guan, J.; Choo, P.; Hu, J.; Smeets, P. J. M.; Odom, T. W. Ultrarapid plasmon resonances from annealed nanoparticle lattices. *Proc. Natl. Acad. Sci. U. S. A.* **2020**, *117* (38), 23380–23384.
- (35) Wang, W.; Watkins, N.; Yang, A.; Schaller, R. D.; Schatz, G. C.; Odom, T. W. Ultrafast Dynamics of Lattice Plasmon Lasers. *J. Phys. Chem. Lett.* **2019**, *10* (12), 3301–3306.
- (36) Liu, J.; Wang, W.; Wang, D.; Hu, J.; Ding, W.; Schaller, R. D.; Schatz, G. C.; Odom, T. W. Spatially defined molecular emitters coupled to plasmonic nanoparticle arrays. *Proc. Natl. Acad. Sci. U. S. A.* **2019**, *116* (13), 5925–5930.
- (37) Sample, A. D.; Guan, J.; Hu, J.; Reese, T.; Cherqui, C. R.; Park, J.-E.; Freire-Fernandez, F.; Schaller, R. D.; Schatz, G. C.; Odom, T. W. Strong Coupling Between Plasmons and Molecular Excitons in Metal-Organic Frameworks. *Nano Lett.* **2021**, *21*, 7775–7780.
- (38) Guan, J.; Sagar, L. K.; Li, R.; Wang, D. Q.; Bappi, G.; Wang, W. J.; Watkins, N.; Bourgeois, M. R.; Levina, L.; Fan, F. J.; Hoogland, S.; Voznyy, O.; de Pina, J. M.; Schaller, R. D.; Schatz, G. C.; Sargent, E. H.; Odom, T. W. Quantum Dot-Plasmon Lasing with Controlled Polarization Patterns. *ACS Nano* **2020**, *14* (3), 3426–3433.
- (39) Guan, J.; Sagar, L. K.; Li, R.; Wang, D. Q.; Bappi, G.; Watkins, N. E.; Bourgeois, M. R.; Levina, L.; Fan, F. J.; Hoogland, S.; Voznyy, O.; de Pina, J. M.; Schaller, R. D.; Schatz, G. C.; Sargent, E. H.; Odom, T. W. Engineering Directionality in Quantum Dot Shell Lasing Using Plasmonic Lattices. *Nano Lett.* **2020**, *20* (2), 1468–1474.
- (40) Li, R.; Bourgeois, M. R.; Cherqui, C.; Guan, J.; Wang, D. Q.; Hu, J. T.; Schaller, R. D.; Schatz, G. C.; Odom, T. W. Hierarchical Hybridization in Plasmonic Honeycomb Lattices. *Nano Lett.* **2019**, *19* (9), 6435–6441.
- (41) Knudson, M. P.; Li, R.; Wang, D. Q.; Wang, W. J.; Schaller, R. D.; Odom, T. W. Polarization-Dependent Lasing Behavior from Low-Symmetry Nanocavity Arrays. *ACS Nano* **2019**, *13* (7), 7435–7441.
- (42) Wang, D. Q.; Bourgeois, M. R.; Lee, W. K.; Li, R.; Trivedi, D.; Knudson, M. P.; Wang, W. J.; Schatz, G. C.; Odom, T. W. Stretchable Nanolasing from Hybrid Quadrupole Plasmons. *Nano Lett.* **2018**, *18* (7), 4549–4555.
- (43) Yang, A. K.; Huntington, M. D.; Cardinal, M. F.; Masango, S. S.; Van Duyne, R. P.; Odom, T. W. Hetero-oligomer Nanoparticle Arrays for Plasmon-Enhanced Hydrogen Sensing. *ACS Nano* **2014**, *8* (8), 7639–7647.
- (44) Yang, A. K.; Hoang, T. B.; Dridi, M.; Deeb, C.; Mikkelsen, M. H.; Schatz, G. C.; Odom, T. W. Real-time tunable lasing from plasmonic nanocavity arrays. *Nat. Commun.* **2015**, *6*, 6939.

- (45) Shi, L.; Hakala, T. K.; Rekola, H. T.; Martikainen, J. P.; Moerland, R. J.; Torma, P. Spatial Coherence Properties of Organic Molecules Coupled to Plasmonic Surface Lattice Resonances in the Weak and Strong Coupling Regimes. *Phys. Rev. Lett.* **2014**, *112* (15), 153002.
- (46) Ramezani, M.; Le-Van, Q.; Halpin, A.; Rivas, J. G. Nonlinear Emission of Molecular Ensembles Strongly Coupled to Plasmonic Lattices with Structural Imperfections. *Phys. Rev. Lett.* **2018**, *121* (24), 243904.
- (47) Berghuis, A. M.; Halpin, A.; Quynh, L. V.; Ramezani, M.; Wang, S. J.; Murai, S.; Rivas, J. G. Enhanced Delayed Fluorescence in Tetracene Crystals by Strong Light-Matter Coupling. *Adv. Funct. Mater.* **2019**, *29* (36), 1901317.
- (48) Spanopoulos, I.; Hadar, L.; Ke, W. J.; Tu, Q.; Chen, M.; Tsai, H.; He, Y. H.; Shekhawat, G.; Dravid, V. P.; Wasielewski, M. R.; Mohite, A. D.; Stoumpos, C. C.; Kanatzidis, M. G. Uniaxial Expansion of the 2D Ruddlesden-Popper Perovskite Family for Improved Environmental Stability. *J. Am. Chem. Soc.* **2019**, *141* (13), 5518–5534.
- (49) Lee, M. H.; Huntington, M. D.; Zhou, W.; Yang, J. C.; Odom, T. W. Programmable Soft Lithography: Solvent-Assisted Nanoscale Embossing. *Nano Lett.* **2011**, *11* (2), 311–315.
- (50) Henzie, J.; Kwak, E. S.; Odom, T. W. Mesoscale metallic pyramids with nanoscale tips. *Nano Lett.* **2005**, *5* (7), 1199–1202.
- (51) Gao, H. W.; Henzie, J.; Odom, T. W. Direct evidence for surface plasmon-mediated enhanced light transmission through metallic nanohole arrays. *Nano Lett.* **2006**, *6* (9), 2104–2108.
- (52) Yang, A.; Hryn, A. J.; Bourgeois, M. R.; Lee, W. K.; Hu, J.; Schatz, G. C.; Odom, T. W. Programmable and reversible plasmon mode engineering. *P Natl. Acad. Sci. USA* **2016**, *113* (50), 14201–14206.
- (53) Guo, R.; Hakala, T. K.; Torma, P. Geometry dependence of surface lattice resonances in plasmonic nanoparticle arrays. *Phys. Rev. B* **2017**, *95* (15), 155423.
- (54) Baranov, D. G.; Wersäll, M.; Cuadra, J.; Antosiewicz, T. J.; Shegai, T. Novel Nanostructures and Materials for Strong Light–Matter Interactions. *ACS Photonics* **2018**, *5* (1), 24–42.
- (55) Yuan, M. J.; Quan, L. N.; Comin, R.; Walters, G.; Sabatini, R.; Voznyy, O.; Hoogland, S.; Zhao, Y. B.; Beauregard, E. M.; Kanjanaboos, P.; Lu, Z. H.; Kim, D. H.; Sargent, E. H. Perovskite energy funnels for efficient light-emitting diodes. *Nat. Nanotechnol.* **2016**, *11* (10), 872.
- (56) Williams, O. F.; Guo, Z. K.; Hu, J.; Yan, L.; You, W.; Moran, A. M. Energy transfer mechanisms in layered 2D perovskites. *J. Chem. Phys.* **2018**, *148* (13), 134706.
- (57) DelPo, C. A.; Kudisch, B.; Park, K. H.; Khan, S. U. Z.; Fassioli, F.; Fausti, D.; Rand, B. P.; Scholes, G. D. Polariton Transitions in Femtosecond Transient Absorption Studies of Ultrastrong Light-Molecule Coupling. *J. Phys. Chem. Lett.* **2020**, *11* (7), 2667–2674.
- (58) Zhang, Z. Y.; Wang, H. Y.; Li, K. J.; Xu, M.; Wang, H.; Gao, B. R.; Chen, Q. D.; Sun, H. B. Perovskite-Cavity Complex: the Modulated Optical Characteristics of Organometallic Halide Perovskite CH₃NH₃PbI_xCl_{3-x} Doped in Length Tunable Optical Microcavities. *J. Phys. Chem. C* **2016**, *120* (24), 13295–13302.
- (59) Hintermayr, V. A.; Polavarapu, L.; Urban, A. S.; Feldmann, J. Accelerated Carrier Relaxation through Reduced Coulomb Screening in Two-Dimensional Halide Perovskite Nanoplatelets. *ACS Nano* **2018**, *12* (10), 10151–10158.
- (60) Cao, Z.; Hu, F.; Zhang, C.; Zhu, S.; Xiao, M.; Wang, X. Optical studies of semiconductor perovskite nanocrystals for classical optoelectronic applications and quantum information technologies: a review. *Advanced Photonics* **2020**, *2* (5), No. 054001.
- (61) deQuilettes, D. W.; Vorpahl, S. M.; Stranks, S. D.; Nagaoka, H.; Eperon, G. E.; Ziffer, M. E.; Snaith, H. J.; Ginger, D. S. Impact of microstructure on local carrier lifetime in perovskite solar cells. *Science* **2015**, *348* (6235), 683–686.
- (62) Liu, N.; Liu, P. F.; Zhou, H. P.; Bai, Y.; Chen, Q. Understanding the Defect Properties of Quasi-2D Halide Perovskites for Photovoltaic Applications. *J. Phys. Chem. Lett.* **2020**, *11* (9), 3521–3528.
- (63) Avramenko, A. G.; Rury, A. S. Quantum Control of Ultrafast internal Conversion Using Nanoconfined Virtual Photons. *J. Phys. Chem. Lett.* **2020**, *11* (3), 1013–1021.
- (64) Deng, S. K.; Li, R.; Park, J. E.; Guan, J.; Choo, P.; Hu, J. T.; Smeets, P. J. M.; Odom, T. W. Ultranarrow plasmon resonances from annealed nanoparticle lattices. *P Natl. Acad. Sci. USA* **2020**, *117* (38), 23380–23384.